1 **GNSS Radio Occultation Soundings from Commercial Off-the-Shelf Receivers Onboard Balloon**

2 **Platforms**

3 Kevin J. Nelson[1, *], Feiqin Xie[1], Bryan C. Chan[2], Ashish Goel[2], Jonathan Kosh[2], Tyler G. R. Reid[2],
4 Corey R. Snyder[2], Paul M. Tarantino[2]

6 [1] Texas A&M University – Corpus Christi, Corpus Christi, TX, USA

7 [2] Night Crew Labs, LLC, Woodside, CA, USA

8 [*] Author now at Jet Propulsion Laboratory, California Institute of Technology, Pasadena, CA: kevin.j.nelson@jpl.nasa.gov

9 **Abstract**

10 *The global Navigation Satellite System (GNSS) radio occultation (RO) technique has*

11 *proven to be an effective tool for Earth atmosphere profiling. Traditional spaceborne RO*

12 *satellite constellations are expensive with relatively low sampling density for specific regions of*

13 *interest. In contrast, airborne RO platforms can provide much higher spatial and temporal*

14 *sampling of ROs around regional weather events. This study explores the capability of a low-cost*

15 *and scalable Commercial-Off-The-Shelf (COTS) GNSS receiver onboard high-altitude balloons.*

16 *The refractivity retrievals from balloon-borne RO payloads obtained from two flight campaigns*

17 *(World View and ZPM-1) are presented. The balloon-borne RO soundings from the World View*

18 *campaign show refractivity profiles between 6 and 19 km with overall near-zero median*

19 *difference from colocated ECMWF ERA5 reanalysis data and variability comparable to*

20 *spaceborne RO missions (~2.3% median-absolute-deviation). Soundings from the ZPM-1*

21 *campaign show a relatively large positive refractivity bias (~2.5%). In summary, low-cost COTS*

22 *RO payloads onboard balloon platforms are worth further engineering and study in order to*

23 *provide capabilities for dense, targeted atmospheric soundings that can improve regional*

24 *weather forecasts via data assimilation.*

Deleted: high-quality

Deleted: the

27 **1. Introduction**

28   The radio occultation (RO) atmospheric profiling method was first developed to

29 measure planetary atmospheres in our solar system. The first major use of RO was part of the

30 mission to examine atmospheric profiles of Venus as part of the Mariner V mission launched in

31 1967 (Fjeldbo and Eshleman, 1969; Fjeldbo et al., 1971). Due to vertical atmospheric density

32 gradients, radio signals transmitted from the spacecraft will bend and be slightly delayed when

33 passing through the limb of the planetary atmosphere before arriving at a receiving antenna on

34 Earth. This bending accumulation along the ray path can be precisely measured using excess

35 phase, and can be used to derive atmospheric pressure, temperature, and concentration of

36 atmospheric constituents (e.g., sulfuric acid concentrations on Venus). The same method was

37 later applied to Mars (Mariner IX, Kliore et al., 1972; Lindal et al., 1979) and Neptune (Voyager

38 II, Lindal, 1992). Even as recently as 2017, additional RO missions to Venus were underway

39 (AKATSUKI, Imamura et al., 2017).

40   It was not until the mid-1990s that scientists began to apply RO techniques to the

41 Earth's atmosphere using Global Navigation Satellite System (GNSS) signals as transmitting

42 sources (Kursinski et al., 1996, 1997; Ware et al., 1996). To date, most Earth GNSS RO

43 observations are taken from low-Earth orbiting (LEO) satellite constellations such as the

44 Constellation Observing System for Meteorology, Ionosphere, and Climate (COSMIC-1, Anthes

45 et al., 2008), the GNSS Receiver for Atmospheric Sounding (GRAS, Luntama et al., 2008)

46 onboard the MetOp satellite series, and COSMIC-2 (Schreiner et al., 2020). More recently,

47 several private companies (e.g., Spire, GeoOptics, PlanetiQ) launched CubeSat constellations

48 that can offer RO soundings with comparable quality to the more sophisticated satellite RO

50   missions (Bowler, 2020). The impact of spaceborne RO profile assimilation on global weather

51   forecasts has been ranked second among satellite measurements (Cardinali and Healy, 2014),

52   with its impact varying depending on assimilation methods (Boullot et al., 2014; Harnisch et al.,

53   2013; Ruston and Healy, 2020).

54   RO observations are also possible from receivers inside the atmosphere, as opposed to

55   from the LEO receivers in space. One of the more common in-atmosphere RO platforms is an

56   airplane or drone. Airborne radio occultation (ARO) typically uses custom-built receiver

57   payloads onboard a modified aircraft with additional antennae and is capable of significantly

58   higher spatial sampling density than spaceborne RO (Wang et al., 2016) due to their slower

59   velocities compared to the LEO receiver satellites (e.g., COSMIC-1, COSMIC-2). This allows ARO

60   receivers to potentially track more GNSS signals, creating the potential for more frequent,

61   localized occultations (Chan et al., 2021, 2022; Xie et al., 2008). ARO platforms also have the

62   benefit of providing on-demand RO profiles around transient weather events such as mid-

63   latitude or tropical cyclones. ARO is limited primarily by flight restrictions regulated by aviation

64   safety agencies (e.g., U.S. Federal Aviation Administration, European Union Aviation Safety

65   Agency), and by fuel range of the aircraft. In addition, the slower-moving airborne receivers

66   lead to longer occultation duration with increased tangent point drifting distance, potentially

67   leading to larger variations in the sampled atmosphere in comparison with the spaceborne RO.

68   Early ARO studies developed and tested research instruments as a baseline for in-

69   atmosphere RO, and modified the traditional spaceborne RO retrieval algorithms (Garrison et

70   al., 2007; Healy et al., 2002; Xie et al., 2008; Zuffada et al., 1999). Open-loop signal tracking

71   algorithms were successfully implemented to reduce unwrapping and tracking errors from

74 airborne platforms (Murphy et al., 2015; Wang et al., 2016). Radio-holographic retrieval

75 methods modified for in-atmosphere radio occultations (Adhikari et al., 2016; Wang et al.,

76 2016) have also been implemented to improve upon geometric optics retrievals (Kursinski et

77 al., 1997, 2000) in the moist lower troposphere to reduce multi-path errors.

78   Another option for an RO observation platform is a high-altitude balloon, but few

79 attempts have been successfully implemented thus far. The Concordiasi Project (Rabier et al.,

80 2013, 2010) is the only field campaign to date during which balloon-borne RO (BRO)

81 observations were targeted as part of the overall research goal. Haase et al., (2012) detailed the

82 proof-of-concept BRO payload and platform design, along with some preliminary results

83 indicating the feasibility of BRO measurements from the Concordiasi field campaign. More

84 recently, Cao et al., (2022) showed that BRO using a custom-built receiver payload aboard a

85 high-altitude Strateole-2 balloon (Haase, J. S. et al., 2018) is also capable of resolving equatorial

86 Kelvin waves. Other remote sensing projects have used balloon platforms for other purposes

87 (e.g., GNSS Reflectometry (GNSS-R), Carreno-Luengo et al., 2016) but GNSS RO payloads on

88 balloon platforms are still otherwise underrepresented.

89   Balloon-borne RO has many advantages over spaceborne RO and ARO. Like ARO

90 observations, BRO platforms move slowly compared to spaceborne platforms, and are

91 therefore capable of offering high spatial and temporal sounding densities over targeted

92 regions. Additionally, BRO platforms can remain aloft and collect observations for weeks to

93 months, depending on the design and capabilities of the platforms (Chan et al., 2021, 2022).

94 BRO platforms can also be tactically launched *en masse* above and around transient weather

95 events such as tropical cyclones and supercell thunderstorms to provide spatially dense

96   sampling of atmospheric thermodynamic profiles inside and surrounding dangerous weather

97   events.

98   Multiple U.S. federal agencies have also invested in supplementary RO data to support

99   operational weather forecast. The U.S. National Oceanic and Atmospheric Administration

100   (NOAA) is undergoing a multi-year program intended to incentivize commercial participation in

101   data-as-a-service that can be used for improving weather forecasting through data assimilation

102   (National Oceanic and Atmospheric Administration and National Environmental Satellite, Data,

103   and Information Service, 2020). The U.S. National Aeronautics and Space Administration (NASA)

104   also funds a Commercial Smallsat Data Acquisition (CSDA) Program (NASA CSDA, 2023), of

105   which RO profiles are an area of heavy research. Furthermore, low-cost, on-demand RO data

106   would be highly useful for conducting research in the planetary boundary layer (PBL), a

107   targeted observable in the NASA 2017 decadal survey (National Academies of Sciences, 2018).

108   BRO data could be a low-cost alternative or supplement to spaceborne and airborne radio

109   occultation data for PBL sensing.

110   The remainder of this paper is structured as follows. Section 2 briefly introduces a newly

111   developed, low-cost and scalable COTS GNSS receiver onboard high-altitude balloons and the

112   associated flight campaigns, along with the detailed description on BRO data and methodology.

113   Section 3 shows the refractivity retrieval process and quality control procedures based on one

114   representative BRO case. Section 4 examines the overall statistics of the BRO observations and

115   provides a preliminary error analysis. Finally, conclusions and future studies are summarized in

116   Section 5.

117   **2. Data and Methodology**

119   **a. Balloon-borne GNSS RO Payload and High-altitude Balloon Platforms**

120   A detailed description of the balloon-borne GNSS RO payload developed by Night Crew

121 Labs (NCL) can be found in (Chan et al., 2021, 2022) – a summary is presented here. The

122 instrumentation is comprised of two major components: a mission system support component,

123 and a science payload for GNSS RO profiling. The mission system support component is the

124 Balloon Re-Programmable Integrated Computer (BRIC), which is a third-generation flight

125 management computer supporting data logging as well as power management, flight control,

126 and thermal control. The science payload is the GNSS Radio Occultation and Observable Truth

127 (GROOT), which is a first-generation balloon-borne GNSS RO science instrument based on COTS

128 GNSS equipment. The GROOT payload includes a Swift Navigation Piksi Multi GNSS receiver for

129 raw RO measurements (e.g., carrier phase, SNR, and Doppler velocities), a Trimble BX992 dual-

130 antenna GNSS receiver coupled with an inertial navigation system and an L-band GNSS

131 corrections service, in addition to the BRIC flight computer and other ancillary needs. All

132 balloon-borne RO data described in this study were collected from the GROOT payload. The

133 Piksi GNSS RO receiver is particularly noteworthy, as it is about the size of a credit card, which is

134 quite small compared to most other custom-built GNSS RO receivers for in-atmosphere and

135 spaceborne observations.

Deleted: airborne
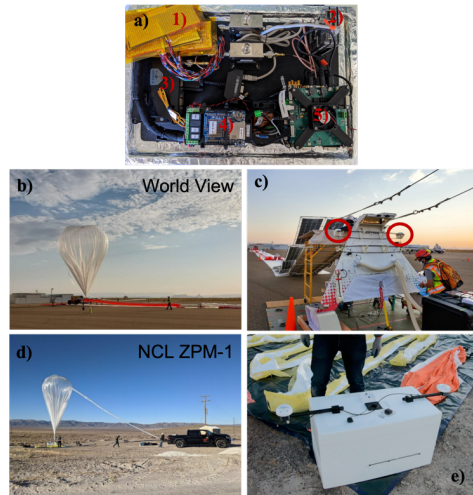
137
138 *Figure 1: a) GROOT payload used in balloon RO flight missions. Numbers indicate the following components – 1) Patch heaters,*
139 *2) Raspberry Pi data logger, 3) Trimble BX992 receiver, 4) BRIC flight computer, 5) Power board/Swift Piksi Multi stack for phase*
140 *and amplitude measurements (adapted from Chan et al., (2022)); b) World View Stratolite balloon being filled prior to launch. c)*
141 *Balloon RO payload being prepared for launch during World View BRO flight campaigns. GNSS antennae are indicated by red*
142 *circles. d) NCL ZPM balloon being filled prior to launch. e) ZPM-1 RO payload and GNSS antennae configuration.*

143   In this study, the RO profiles collected from two high-altitude balloon flight campaigns

144 equipped with the GROOT payload were analyzed. Figure 1a shows the GROOT payload as

145 described above, with each component labeled. The first of a series of high-altitude balloon

146 campaigns occurred in August 2020 on a zero-pressure balloon as a secondary payload hosted

147 on the World View Stratolite balloon bus platform (Fig. 1b, c). The World View flight launched

148 out of Page, AZ and maintained 18+ km (60,000+ ft) altitude, enabling five days (120 hours) of

149 continuous data collection. During the flight, GROOT continuously collected balloon state data

150 and RO data from the GPS (United States), GLONASS (Russia), Galileo (European Union), BeiDou

151 (China), and QZSS (Japan) constellations. The World View balloon platform was equipped with

152 yaw control equipment to minimize spinning during flight and to allow for yaw rotation

154 corrections as necessary. After mission termination, the payload was recovered, and the data

155 was processed.

156   The second flight campaign was the NCL Zero Pressure Balloon Mission 1 (ZPM-1), which

157 launched near Empire, NV on November 28, 2020 (Fig. 1d, e). The ZPM-1 balloon reached a

158 maximum altitude of 31.7 km (104,567 ft), traveling southeast toward Utah. Overnight, ZPM-1

159 dropped to a lower-than-expected altitude of 17.9 km (59,000 ft) due to colder ambient

160 temperature, which caused the balloon to drift eastwards towards the Rocky Mountains and

161 led to early termination of the mission after 12 hours. During the flight, GROOT collected

162 balloon state data and RO data from GPS, GLONASS, Galileo, BeiDou and QZSS constellations.

163 The payload was later recovered in southern Utah.

164   **b. Balloon-Borne RO Measurements**

165   Figure 2 shows the ground tracks for the two balloon flight campaigns along with the

166 predicted occultation tangent point locations at the lowest elevation angle, labeled by their

167 respective GNSS RO satellites. The selected occultation events extracted for analysis are

168 highlighted for both flight campaigns.
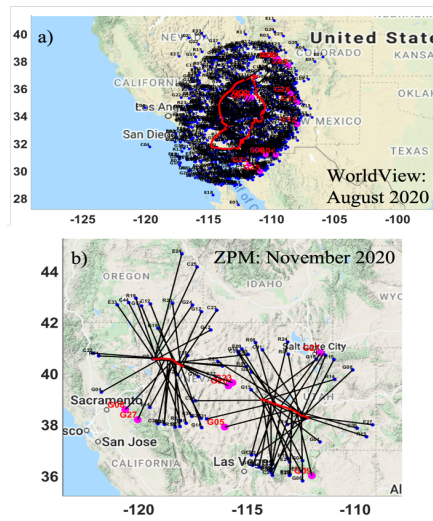
169
170   *Figure 2: High-altitude balloon flight trajectory (red) and predicted occultation tangent point drifting paths and their respective*
171   *GPS satellite numbers (black) for a) World View and b) ZPM-1. Pink circles with red text indicate the selected RO cases and the*
172   *occulting GPS satellite number presented in this study.*

173   The GROOT receiver can potentially track all currently operational GNSS satellite constellations

174   such as GPS, GLONASS, Galileo, BeiDou, and QZSS. Out of a total number of 680 predicted

175   occultation soundings for the World View flight (based on balloon and GNSS real trajectories),

176   approximately 71% of observations came from non-GPS occultations and were not analyzed

177   (see Fig. A1). This decision was made because GROOT processing on non-GPS satellites data

178   from several previous flights consistently resulted in poor quality ROs as a result of receiver

179   bandwidth limitations. In addition, the closed-loop tracking receiver in the GROOT payload can

180   only track setting (vs. rising) occultations, filtering out another 50% of the available

181   occultations. Of the remaining occultations, only the RO events having measurements with 1)

182   minimum elevation angle less than 0°, and 2) excess phase greater than 50 meters were

183   processed. This subset of occultations were divided into those that are good quality and those

186   that require additional quality control such as cycle-slip corrections (Fig. A1). Of the original 680

187   occultations from the World View flight, only 15 cases were extracted for analysis (see

188   Appendix A). Cycle slip corrections were required for 7 of the 15 cases, and one World View

189   case was removed after failing quality control procedures. The same pre- and post-processing

190   algorithms were applied to ZPM-1 measurements. Unfortunately, the ZPM-1 flight encountered

191   power failures during the segments of the flight, resulting in the loss of altitude and a much

192   shorter flight time with fewer occultations being collected, and only 8 occultations out of 84

193   were selected for processing.

194   c.   **Balloon-Borne RO Data Processing and Retrieval Methods**

195   After the flight data is logged, several pre-processing steps are required prior to

196   retrieving bending angle and refractivity. The full retrieval process is detailed in (Chan et al.,

197   2022), but is summarized here. The first step in the BRO retrieval is to pre-process the L1

198   frequency data for ingestion into the retrieval algorithms. Raw line-of-sight (LOS) GNSS

199   observables, along with satellite ephemeris data, and balloon state (position/velocity) data, all

200   of which are measured at 10 Hz, are extracted from payload storage. Once the LOS data is

201   parsed and aligned, the next step is to compute the excess phase by subtracting the receiver's

202   measured phase from the LOS geometric distance between the occulting GNSS satellite and the

203   receiver. Step three is receiver clock calibration, where the excess phase is calibrated by

204   differencing the excess phase of the occulting and high-elevation GNSS satellites. Step four is

205   cycle slip correction, where an exponential curve is fitted to the data to both smooth and

206   remove medium to large discontinuities. Step five uses a Gaussian Process Regression (GPR, Shi

207   and Choi, 2011) to further remove any smaller discontinuities as needed in processing the

210   individual cases. Steps three through five clean and smooth the excess phase data so that it can

211   be used in the retrieval downstream in the retrieval processing. Finally, the pre-processed

212   results, RO excess phase, excess Doppler shift, SNR, and balloon state, are exported as a

213   NetCDF file, a format convenient for downstream GNSS RO retrieval processing. In our study,

214   the L2 frequency data was often less reliable for retrievals as it would often drop out sooner

215   than the L1 data. However, the L2 data was still used for pre-processing data corrections (e.g.

216   data verification, cycle-slip corrections).
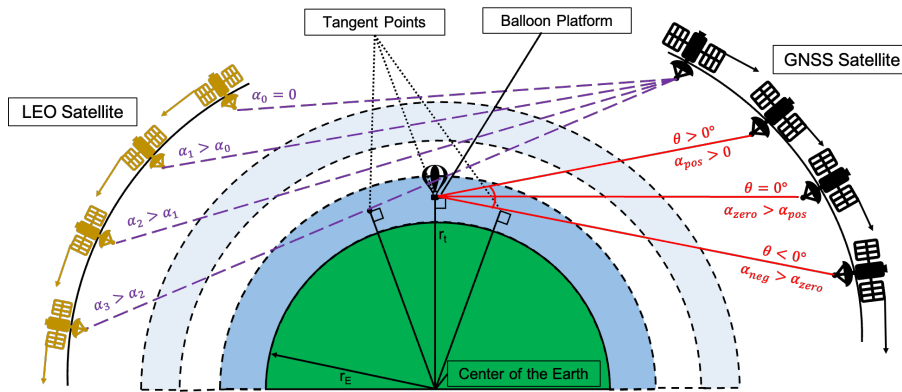
217
218   Figure 3: Balloon radio occultation transmitter/receiver geometry diagram without showing the bending of the GNSS ray paths.
219   r_E and r_t represent the radius of the earth and the radius at the tangent point, respectively. Adapted from (Xie et al., 2008).

220   Unlike the well-known traditional spaceborne RO, balloon-borne (and airborne) RO have

221   a more unique, less common transmitter/receiver geometry (Figure 3). The receiver onboard

222   the balloon platform is shown in the center at a radius r_t. High-elevation GNSS satellites, where

223   the elevation angle is required to be $\theta > 55°$, are used to calibrate the excess phase at the in-

224   atmosphere receiver. GNSS satellites with elevation angle $-5° < \theta < 5°$ are used in the retrieval

225   process to calculate the bending angle retrievals and subsequent products (Xie et al., 2018;

226   Chan et al., 2022).

232   To evaluate the performance of the balloon-borne GNSS-RO retrieval algorithm, an end-

233   to-end simulation and retrieval processing system (Figure 4) originally developed for aircraft-

234   based GNSS RO (Xie et al., 2008) was adapted for balloon-borne RO measurements. The

235   processing system includes four main components: (a) a geometric optics ray-tracer, i.e., Radio

236   Occultation Simulations for Atmospheric Profiling (ROSAP, Høeg et al., 1996), which simulates

237   the GNSS RO signal and calculates the associated excess phase and excess Doppler as well as

238   the along-path accumulated bending angle at each impact parameter as it travels through a

239   prescribed Earth's atmosphere (with either spherical or oblate Earth) given by a 1-dimensional

240   atmospheric refractivity profile. The oblate Earth option is used in our study; (b) a module that

241   derives the bending angle from the LOS excess phase/Doppler measurements through a

242   modified geometric-optics (GO) retrieval, i.e., Doppler-to-alpha, (Lesne et al., 2002; Vorob'ev

243   and Krasil'nikova, 1994; Xie et al., 2008) and radio-holographic retrieval (i.e., FSI, Jensen et al.,

244   2003) modified for in-atmosphere retrievals (Adhikari et al., 2016); (c) a forward Abel integrator

245   (FAI) modified for in-atmosphere RO retrievals that generates the bending angle profile through

246   the forward integration of an input refractivity profile (Fjeldbo and Eshleman, 1969; Fjeldbo et

247   al., 1971; Xie et al., 2008); and (d) an inverse integrator that retrieves a refractivity profile via an

248   Inverse Abel Transform (IAT, Fjeldbo and Eshleman, 1969) modified for in-atmosphere RO

249   (Healy et al., 2002; Xie et al., 2008). Note that the GO retrieval method has limited vertical

250   resolution and encounters multipath problems in the moist lower troposphere. Therefore, the

251   FSI method adapted for airborne and balloon-borne RO retrieval will also be used (Adhikari et

252   al., 2016).

Deleted: ray path

Deleted: its

Deleted: delay

Deleted: /

Deleted: , and

Deleted: by a

259
260
261
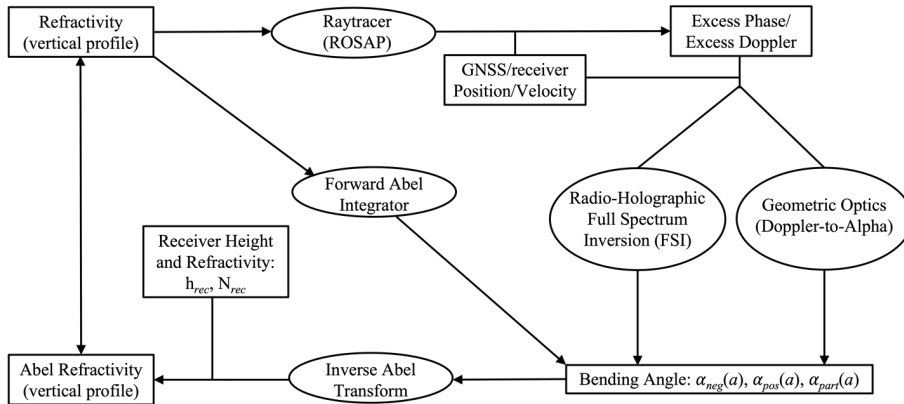
Figure 4: Flow chart of the end-to-end simulation and retrieval processing system for airborne and balloon-borne GNSS radio occultation.

262   During the retrieval process, the pre-processed 10 Hz LOS observations are log-linearly

263   smoothed using a 30 second moving window to further ensure that high-frequency noise has

264   been removed. The ROSAP simulation also runs its ray-tracing at the same sampling interval as

265   the provided satellite/receiver geometry. The excess phase output of the ROSAP simulation is

266   also run through the same log-linear smoothing algorithm as the LOS excess phase.

267   After the bending angle (α) profiles are retrieved using either GO or FSI methods, the

268   partial bending angle (α_{part}), i.e., the difference between negative and positive elevation

269   bending angles (α_{neg} and α_{pos}, respectively) at the same impact parameter, can be derived. The

270   partial bending angle profile is then converted to the refractivity profile using the modified IAT,

271   which requires *a priori* knowledge of the refractivity at the receiver during the occultation

272   event. In addition, the local radius of curvature of the Earth (r_E) is also required for conversion

273   of bending angle impact parameter to geometric height as part of the IAT. Due to the very low

274   excess phase, the raw observation of α_{pos} as well as the α_{neg} near the receiver height is generally

275   very small and can also be rather noisy, which would lead to large errors in partial bending

277   angle and the following refractivity retrieval. Therefore, in this study, the α_{pos} and the α_{neg}

278   within 1.5 km of the receiver altitude were substituted by the simulated bending angle (e.g., FAI

279   or ROSAP bending angle simulation) based on a colocated refractivity profile (Adhikari et al.,

280   2016; Xie et al., 2018). By doing this, the top 1.5 km of the α_{pos} and the α_{neg} profiles are

281   significantly less noisy, preventing failure of the IAT.

282   **d. ERA5 Model Reanalysis Data**

283   To evaluate the quality of balloon-borne RO measurements, we use 3-hourly ERA5

284   model reanalysis (Hersbach et al., 2020) from the European Centre for Medium-range Weather

285   Forecasting (ECMWF) to provide estimates of atmospheric conditions near the BRO sounding

286   locations. The native ERA5 model grid has 0.25°x0.25° horizontal resolution and 137 vertical

287   levels. The ERA5 profiles are referenced to geopotential heights, which are converted to

288   geometric heights for direct comparisons to BRO profiles. The ERA5 atmospheric refractivity

289   profiles can be derived from the gridded temperature, water vapor pressure (humidity), and

290   pressure profiles according to Equation 1.

291       $$N = a_1 \frac{P}{T} + a_2 \frac{P_w}{T^2} \tag{1}$$

292   Equation 1 is an approximation of atmospheric refractivity for the neutral atmosphere where N

293   is refractivity in [N-units], P is atmospheric pressure in [hPa], T is atmospheric temperature in

294   [K], P_w is the water vapor pressure in [hPa], and a_1 and a_2 are unitless coefficients with values of

295   77.6 and 3.73x10^5, respectively (Kursinski et al., 1997, 2000).

296   In addition, during an occultation event, the tangent point (TP) is located at the receiver

297   position, when the occulting satellite is at the zero elevation. In-atmosphere RO bending angle

298   retrieval requires *a priori* atmospheric refractivity at the receiver, which can be provided by a

302   colocated ERA5 profile, when high-quality in-situ measurements are not available (Xie et al.,

303   2018, 2008; Adhikari et al., 2016). Thus, each occultation event uses one referencing refractivity

304   profile from the colocated ERA5 grid at the zero-elevation ($\theta = 0$) angle tangent point location.

305   This refractivity profile is used to compute the time series of refractivity at the receiver

306   throughout the occultation observations by interpolating the refractivity profile to the receiver

307   height at each time stamp. Furthermore, considering the high horizontal resolution of ERA5

308   reanalysis and the potential fine scale variations of refractivity that are smaller than RO

309   horizontal footprint, we use a median refractivity profile of a 1°x1° horizontal grid surrounding

310   the zero-elevation TP location for input into the initial ROSAP and FAI simulations. The tangent

311   point locations during the occultation event can therefore be derived from ROSAP ray-tracing

312   simulation with the real occultation geometry. It is important to consider the relatively large

313   horizontal drift of BRO TPs when determining the accuracy of the retrieved refractivity profiles.

314   To best evaluate the quality of the individual retrieved BRO refractivity profiles, the final

315   refractivity comparison uses the ERA5 profile at the 5 km TP location determined by the initial

316   ROSAP simulations. Therefore, three separate refractivity profiles from ERA5 are used during

317   the retrieval process: the zero-elevation angle refractivity profile for the time series of

318   refractivity at the receiver, the 1°x1° median refractivity profile surrounding the zero-elevation

319   angle location used for input into simulations, and the 5 km TP location refractivity profile used

320   for final retrieval comparisons.

321   **3. Case Study: BRO from the World View Campaign**

Deleted: for simplicity,

Deleted: tter

Deleted: will be treated as the BRO colocated profile for the final refractivity comparison.
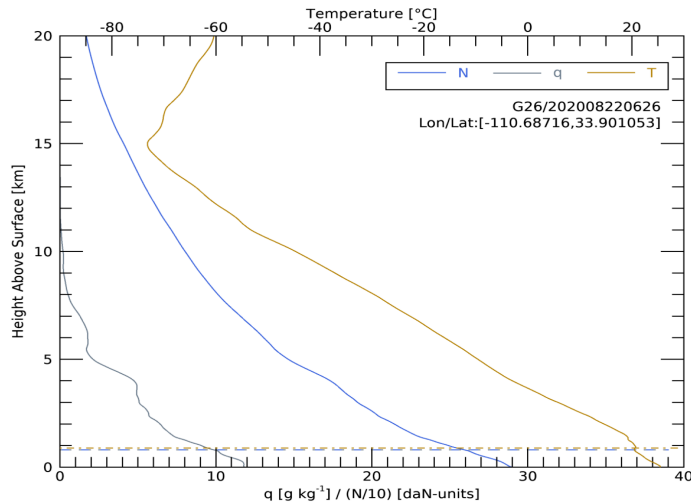
Figure 5: ERA5 vertical profiles of temperature (T, gold), specific humidity (q, grey), and refractivity (N, blue) at 0600 UTC colocated with the World View G26 BRO case on August 22, 2020. Note that for display purposes, one-tenth of the refractivity (N/10) was plotted. In addition, the colocation longitude and latitude of the BRO profile are indicated. Dashed lines indicate the planetary boundary layer height (PBLH) as determined by the gradient method from each variable (see text for details).

331   Here we focus on one typical BRO sounding, an approximately 27-minute-long BRO

332   measurement from the World View campaign (hereafter referred to as WVG26) at 06:26 UTC,

333   August 22, 2020. The WVG26 case occurred over the Tonto National Forest, northeast of

334   Phoenix, Arizona. The colocated (zero-elevation angle location) ERA5 thermodynamic profiles

335   (temperature, specific humidity, and refractivity) at the location of this BRO sounding with

336   tangent point at 5 km above mean-sea-level are shown in Figure 5. During the occultation

337   event, the local atmosphere was hot and very dry, particularly above 5 km. Additionally, the

338   planetary boundary layer height (PBLH) detected using the gradient method (Nelson et al.,

339   2021; Winning et al., 2017; Ao et al., 2008, 2012; Xie et al., 2006) for this case was found to be

340   at approximately 0.9 km, clearly marked by a distinct temperature inversion (gold, dash-dot

Need to be consistent with the "Response" document point#6¶

345   line) and weak vertical gradients in specific humidity (grey, dotted line), and refractivity (blue,

346   dashed line) shown in Fig. 5). The cold-point tropopause was located around 15 km altitude.

347
348   *Figure 6: WVG26 time series of a) excess phase, b) excess Doppler, c) signal-to-noise ratio, and d) elevation angle from*
349   *calibrated observations (blue), and ROSAP ray-tracing simulation (red). Dashed lines in panels a) and b) represent differences*
350   *between the LOS observations and the ROSAP simulation.*

351   Figure 6a shows the WVG26 calibrated excess phase observations (blue) alongside the

352   excess phase from the ROSAP simulation (red) and the difference between the LOS

353   observations and the ROSAP simulation (black dashed line). The calibrated excess phase

354   compares favorably with the corresponding ROSAP excess phase, with differences between the

355   two within three meters of each other throughout the whole time series. The high consistency

356   throughout the time series is also seen in the excess Doppler comparison (Fig. 5b) with

357   differences only exceeding 0.01 m s^{-1} at the end of the time series. The observed L1 signal-to-

Deleted: dashed/dotted lines

Deleted: ,

Deleted: delay

Deleted: delay

Deleted: t

Deleted: delay

Deleted: colocated

Deleted: delay

366   noise ratio (SNR) for the WVG26 case is shown in Figure 6c. As the signal penetrates deeper into

367   the atmosphere (i.e., the elevation angle dipping below the local horizon to approximately –

368   4.5°, Fig. 6d), the SNR typically decreases and becomes much more variable due to high signal

369   dynamics resulting from the fine moisture variations in the lower troposphere. The overall

370   mean L1 SNR from the GROOT receiver (141.79 V V^{-1}) is smaller than the mean SNR from the

371   COSMIC-1 and SAC-C GNSS RO satellite missions (approximately 700 V V^{-1}, Ao et al., 2009; Ho et

372   al., 2020). Although the L1 SNR values from the Piksi receiver are approximately 5 times less

373   than the values from spaceborne RO missions, considering the compact size of the Piksi

374   receiver, such L1 SNR values are quite impressive and can be partially attributed to the smaller

375   defocusing effect compared to that of spaceborne RO as the Piksi receiver is inside the

376   atmosphere.

377   Figure 7a shows the BRO bending angle profiles from GO and FSI retrievals as a function

378   of impact height (impact parameter minus the local curvature radius of the Earth) for the

379   WVG26 case. Note that as discussed in Section 2c, the noisy α_{pos} and α_{neg} within 1.5 km below

380   the receiver height were replaced by the simulated FAI bending angle based on the colocated

381   ERA5 refractivity profile (Fig. 5). Fig. 7a also shows a conceptual calculation of the partial

382   bending angle as discussed in Section 2b. At each impact height, α_{pos} is subtracted from α_{neg} to

383   calculate the partial bending angle (α_{part}), which is later used to retrieve the final refractivity

384   profile. Figure 7b shows the partial bending angle calculated using the method shown in Fig. 7a

385   with 100 m log-linear vertical smoothing applied. It is worth noting that BRO bending angle

386   observations from both the GO and FSI retrievals match the colocated ERA5 FAI and ROSAP

387   simulations quite well from the balloon altitude (just over 18 km) all the way down to impact

397 heights of around 6 km (corresponding to approximately 4 km above MSL). Differences

398 between the retrievals and the ROSAP simulation between 10 and 11 km, as well as between 6

399 and 8 km, are most likely caused by platform yaw instability as discussed in Section 2.1.
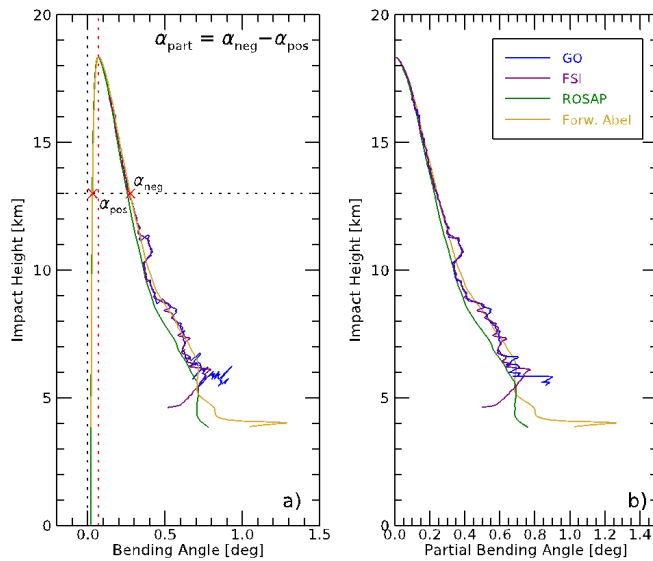
400
401 *Figure 7: a) Bending angle for WVG26 case from the GO retrieval (blue) and FSI retrieval (purple), in comparison with the*
402 *colocated ERA5 bending angle from ROSAP ray-tracing simulation (green), and forward-Abel-integrator (gold). Conceptual*
403 *calculation of partial bending angle at 13 km impact height is also shown. b) Final partial bending angle for WVG26 case from*
404 *the GO retrieval (blue), FSI retrieval (purple), ROSAP ray-tracing simulation (green), and Forward Abel transform (gold).*

405   Figure 8a shows the refractivity retrieval for the WVG26 BRO case. The 5 km tangent

406 height ERA5 refractivity profiles colocated with the WVG26 case is approximately 425 km from

407 the receiver (zero-elevation) location, and the terrain changes significantly compared to the

408 origin point in the Tonto National Forest. From the top of the refractivity profiles, both the GO

409 and FSI retrievals match the ERA5 refractivity profile from the location of the 5 km tangent

410 height very well. Similar to the α_{part} results, the refractivity retrieval from FSI bending angle

411 reaches about 1 km deeper into the atmosphere than the GO retrieval, highlighting the

418   usefulness of the FSI over GO methods. This is primarily due to the improvement from FSI on

419   resolving the multi-path problem over the GO method in the moist lower troposphere.
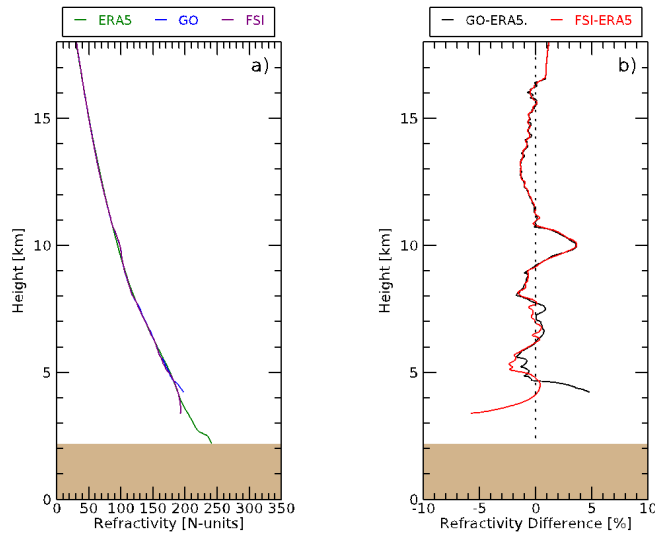
420
421   *Figure 8: a) BRO refractivity retrieval for WVG26 case from GO (blue) and FSI (purple) compared to the colocated refractivity*
422   *profile from ERA5. b) Fractional refractivity difference between BRO retrieval and ERA5 (GO, black; FSI, red). Local terrain at the*
423   *location of BRO tangent point at 5 km above MSL is marked by tan polygons.*

424   In order to quantify the differences between the retrievals and the colocated ERA5

425   profile, the fractional refractivity difference profile is calculated. Figure 8b shows the fractional

426   refractivity difference between the refractivity retrievals and the colocated ERA5 profile,

427   respectively. The GO retrieval is highly consistent with FSI retrieval above ~7.5 km and start

428   showing small differences below. Both retrievals perform very well in the middle troposphere,

429   between 5 km and 10 km. Once more water vapor is encountered below 5 km altitude, the

430   magnitude of the median difference for the GO retrieval increases. Additionally, intermittent

431   signal degradation and loss due to platform yaw rotation likely induces retrieval errors in the

443 FSI retrieval and stops the GO retrieval closer to the surface, resulting in sharp changes in *N*-

444 bias for both retrievals.

4. Evaluation of Balloon-Borne RO Refractivity Retrievals

446   Figure 9 shows the fractional refractivity difference between GO/FSI retrievals and the

447 colocated ERA5 profile for each BRO sounding from the World View flight campaign. Individual

448 fractional refractivity difference profiles are calculated by interpolating the retrieval and ERA5

449 profiles to the same 10 m vertical grid before taking difference between the refractivity

450 profiles. Summary statistics for all World View flight campaign BRO profiles calculated over

451 different height ranges are shown in Table 1. The median refractivity difference between the

452 GO retrieval and the colocated ERA5 oscillates within 0.25% with MAD between 0.71% above

453 15 km and approximately 2.28% across all levels (see Table 1). The GO refractivity retrieval

454 starts
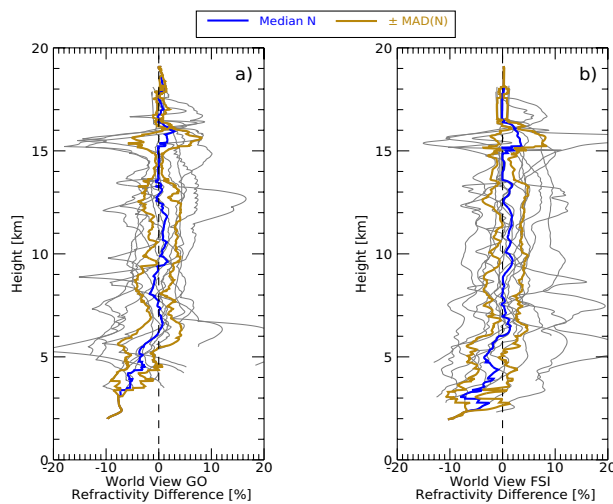
Figure 9: Fractional refractivity difference between BRO retrievals and the colocated ERA5 for: a) GO retrievals and b) FSI retrievals of all World View cases (grey). The median fractional refractivity difference profiles are shown in blue and the median +/- the median absolute deviation (MAD) is shown in gold.

462 showing negative *N*-bias below approximately 6 km, with a median refractivity difference of -

463 5.86% (MAD: 1.99%) over the 0-5 km height range. The FSI retrieval also starts showing

464 negative *N*-bias below approximately 6 km, but with a smaller median difference of -3.60%

465 (MAD: 3.26%). The higher magnitude *N*-bias in the lowest portions of the troposphere have a

466 variety of potential causes. The lowest level negative *N*-bias is likely caused by the tracking

467 errors introduced by the closed-loop tracking receiver, which is a well-known problem that

468 could easily degrade the BRO observation quality (Ao et al., 2009; Wang et al., 2013).

469 Additionally, high spatial variations in moisture content can also cause low SNR or high signal

470 dynamics ultimately resulting in a negative bending angle bias (Wang et al., 2016). It is also

471 important to consider that there is likely to be increased low-sampling bias closer to the

472 surface, weakening the robustness of the statistics.

473
474 *Table 1: Summary statistics for median refractivity differences between GO/FSI retrievals and the colocated ERA5 with corresponding median absolute deviation over varying height ranges from all World View flight campaign BRO profiles.*

Height Range [km]	GO Median *N* Difference [%]	FSI Median *N* Difference [%]
0-5	-5.86 ± 1.99	-3.60 ± 3.26
5-10	-0.25 ±2.97	0.32 ± 3.06
10-15	0.57 ± 2.44	1.06 ± 2.29
15-20	0.53 ± 0.71	0.23 ± 0.94
Overall	0.03 ± 2.28	0.24 ± 2.61

475
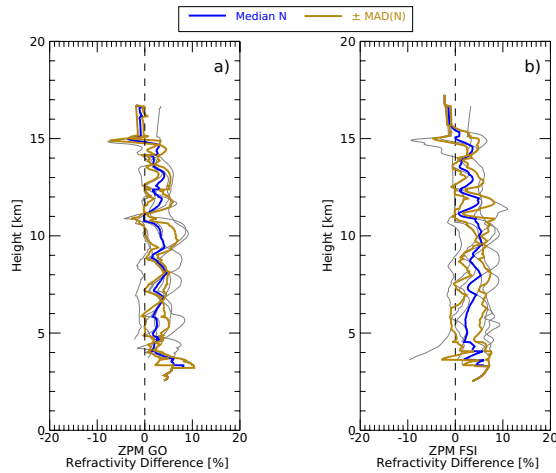
Figure 10: Same as Figure 9, but for the ZPM-1 flight campaign.

Figure 10 shows the fractional refractivity difference profiles for the ZPM-1 flight

campaign from the GO and FSI retrievals. The ZPM-1 refractivity differences are slightly

positively biased overall compared to the World View campaign data. The ZPM-1 refractivity

differences from both retrieval methods show less variability across all heights in both the

median profile and the individual refractivity profiles. The GO retrieval has an overall median

refractivity difference of 2.57% (MAD: 1.38%). The maximum N-bias from the GO retrieval is

4.05% in the lower troposphere. The FSI retrieval has an overall median refractivity difference

of 3.13% (MAD: 2.03%). The World View platform had rotational yaw control capability,

whereas the ZPM-1 platform did not – as such, the platform and GNSS antennae were free to

spin during high-altitude wind gusts. During RO events, rotational movement likely induced

position errors in the dual-antenna navigation system as a result of SNR degradation, which

could potentially result in larger N-bias. Such a phenomenon warrants future investigation of

BRO platform control on BRO retrievals.

499   *Table 2: Same as Table 1, but for the ZPM-1 flight campaign.*

Height Range [km]	GO Median *N* Difference [%]	FSI Median *N* Difference [%]
0-5	4.05 ± 0.99	4.01 ± 2.15
5-10	2.94 ± 1.56	3.59 ± 2.29
10-15	2.57 ± 1.78	3.03 ± 1.73
15-20	-0.94 ± 0.64	-1.33 ± 0.47
Overall	2.57 ± 1.38	3.13 ± 2.03

500

501   Errors in BRO refractivity retrievals can come from a variety of potential sources. One

502   potential cause is the difference in precise orbit determination (POD) solutions for BRO

503   missions. Generally speaking, POD solutions for LEO missions aim to have LEO velocity

504   accuracies of 0.5 mm s^{-1} or better, and LEO position accuracies of 10 cm or better. In contrast,

505   BRO missions are generally capable of velocity accuracies of 30 mm s^{-1} or better, and position

506   accuracies of 5 cm or better. The larger POD velocity errors are due to difficult-to-model

507   disturbances such as wind gusts and other aerodynamic factors. Xie et al., (2008) showed that

508   the addition of simulated of 5 mm s^{-1} random excess Doppler errors will not result in additional

509   *N*-bias, but could possibly introduce less than 1% refractivity error near the receiver (~10 km)

510   and less than 0.2% below ~ 6 km. In the case of our study, the larger BRO receiver positioning

511   errors (if random) will likely not introduce significant *N*-bias (Fig. 9) for World View or ZPM-1

512   cases.

513   As discussed previously, the limitations of closed-loop tracking receivers may also affect

514   the BRO refractivity retrieval quality. Additionally, low SNR in airborne (in-atmosphere) GNSS

515   RO observations can potentially result in approximately ±5% refractivity error (Wang et al.,

516   2016). This estimate is consistent with the overall results showed here, meaning that an

517   improvement to SNR in the lower atmosphere would be extremely beneficial. However, it is

523 important to note that despite the overall positive bias in the ZPM-1 cases, the median absolute

524 deviation of the cases minimizes in the upper and middle troposphere, much like the World

525 View campaign data. One important caveat for the ZPM-1 campaign data is the small number of

526 available occultations. Furthermore, power loss issues on the platform during the flight caused

527 a decrease in the number of occultations. The low sampling numbers could also lead to larger

528 median refractivity differences.

529 **5. Summary and Conclusions**

530   In this study, the GNSS RO atmospheric profiling technique has been adapted for use on

531 high-altitude balloon platforms. Most of the past airborne and balloon-borne RO payloads

532 require custom made parts and costly operational expenses that require significant

533 investments. We show the successful implementation of the Night Crew Labs GROOT payload

534 developed from commercial off-the-shelf (COTS) components on high-altitude balloon

535 platforms. This approach is simpler and significantly more affordable than current airborne and

536 space-based methods. The results from the low-cost, highly compact GROOT payload are

537 promising, but more study is needed.

538   Utilizing a balloon platform for GNSS RO observations has been done only a few times in

539 the past. Haase et al., (2012) showed the proof-of-concept for balloon-borne GNSS RO using a

540 custom-built receiver during the Concordiasi field campaign (Rabier et al., 2010, 2013) and

541 found excess Doppler agreement that would correspond to approximately 1% refractivity

542 difference, indicating that BRO is able to produce high-quality RO profiles. Cao et al., (2022)

543 showed that BRO retrievals can be used to identify equatorial Kelvin waves during long-

544 duration balloon flights with minimal error in the observations. The BRO retrievals from the

Deleted: P

Deleted: s

Deleted: once

548 GROOT payload have refractivity differences in the middle and upper troposphere comparable

549 to previous airborne and balloon-borne RO studies (Adhikari et al., 2016; Haase et al., 2012; Xie

550 et al., 2008; Healy et al., 2002; Cao et al., 2022). The added benefit of using BRO platforms is

551 the dense spatial and temporal sampling over targeted regions due to the low platform

552 velocities relative to the LEO-based RO satellites. Additionally, BRO platforms are scalable and

553 can potentially be launched in advance of significant weather events and remain aloft for long

554 periods of time to collect abundant RO observations.

555   Currently, the major limitation of BRO platforms with COTS payloads is the use of

556 closed-loop tracking GNSS receivers, which limit penetration of RO observations into the lower

557 troposphere due to the large variations in moisture content. Additionally, closed-loop tracking

558 also prohibits the tracking of rising occultations, cutting the potential number of RO soundings

559 in half. For these reasons, design and implementation of COTS payloads capable of open-loop

560 tracking is the next natural step to improving balloon-borne RO. Furthermore, BRO platform

561 orientation can be uncontrolled, so a sudden change in winds aloft can alter the antenna

562 position and cause signal loss. Additionally, the comparatively slow-moving receivers result in

563 longer occultations (approximately 20-30 minutes for one balloon-borne RO event, in

564 comparison to ~1 minute for one spaceborne RO event), which can result in larger unwrapping

565 error (Wang et al., 2016) and lead to further underestimates of bending angle in the moist

566 lower troposphere.

567   An analysis of the quality of the retrieved refractivity profiles reveals that the overall

568 median refractivity difference for the World View campaign is generally less than 1%. The same

569 analysis of the ZPM-1 campaign data shows that the median is slightly positively biased overall

571 (approximately 3%), but with similar median absolute deviation values. While both GO and FSI

572 retrieval methods offer promising results, it appears that the FSI retrievals tend to outperform

573 the GO retrievals in terms of atmospheric penetration. The limitation of the close-loop tracking

574 could be the primary cause of the negative N-bias below 6 km as seen in World View BRO

575 soundings. In addition, the relatively low SNR in the lower troposphere could also lead to

576 negative bending angle bias, which could also be another likely cause of the negative

577 refractivity bias in the lower troposphere.

578 This study shows that high-altitude balloons with RO payloads can be launched over

579 areas of complex terrain, can potentially remain aloft for far longer than airborne RO platforms,

580 and would hypothetically be deployable in all weather conditions, similar to radiosondes.

581 Furthermore, the balloon-borne RO platform can offer unprecedented high spatial and

582 temporal BRO sampling over targeted regions far higher than traditional spaceborne RO (see

583 Fig. 2). Additionally, balloon-borne RO data could be much more cost effective to retrieve due

584 to the low-cost COTS GNSS RO receiver and overall affordability of the high-altitude balloon

585 flight platform, as the instrument can be retrieved and reused after each deployment. We

586 believe the advances on the COTS GNSS RO receiver development and high-altitude balloon

587 platform control in the future will lead to large increases in high-quality localized BRO

588 soundings over targeted weather events (e.g., severe thunderstorms, tropical cyclones, etc.)

589 and improve regional weather forecasts through data assimilation.

590 **6. Acknowledgements**

591 This paper is supported by NOAA grant 1305M2-19-C-NRMW-0015. Author K. Nelson

592 acknowledges the research assistantship support from Coastal Marine System Science Program

Deleted: Overall,

Deleted: we show

595   at Texas A&M University – Corpus Christi. Authors from Night Crew Labs acknowledge

596   additional support from NASA grant 80NSSC20K0106. This work was done as a private venture

597   and not in the authors' capacity as an employee of the Jet Propulsion Laboratory, California

598   Institute of Technology. The authors would also like to thank Dr. Loknath Adhikari from the

599   University of Maryland for productive discussion. The anonymous reviewers are also

600   acknowledged for their insight and comments to improve this paper.

601   **7. Appendix A: Balloon-Borne RO Cases and Sampling**

602   Balloon-borne RO can collect high density observations around the platform, particularly

603   compared to spaceborne RO. Figure A1 shows a Sankey plot filtering visualization of the World

604   View predicted occultations. Onboard the GROOT payload, duplicate Piksi receivers were used

605   to ensure all GNSS constellations were tracked. Piksi 1 was programmed to log data from GPS,

606   Galileo, Glonass, and Beidou, whereas Piksi 2 was only programmed to log data from GPS and

607   Galileo. As such Piksi 2 was able to log more ROs from GPS. We believe the Piksi receivers and

608   antennae were manufactured such that they were tuned to maximize GPS performance, and as

609   such, satellites from the GPS constellation consistently showed better performance than the

610   other constellations.

611   Of the original 680 predicted ROs from all GNSS constellations (originally discussed in

612   section 2.1), a total of 485 were incomplete, and therefore not suitable for retrieval processing.

613   The remaining 195 occultations then filter further by removing those from QZSS, Galileo,

614   BeiDou, and GLONASS with low quality due to the frequency tuning inherent to the Piksi

615   receiver. Of the 167 from the GPS system, only 8 good quality cases were ready to use

616   immediately. Another 7 cases required additional pre-processing in the form of cycle-slip

Moved down [1]: Balloon-borne RO can collect high density observations around the platform, particularly ¶ compared to spaceborne RO. As was discussed in Section in Section 2a, the Piksi GNSS receiver onboard World View balloon could observe a predicted total of 680 potential occultations. Because of frequency restrictions built into the Piksi receiver, signals from GLONASS, BeiDou, QZSS, and Galileo are less reliable due to slight

Moved (insertion) [1]

627   corrections. The same process was also applied for cases observed during the ZPM-1 flight

628   campaign.
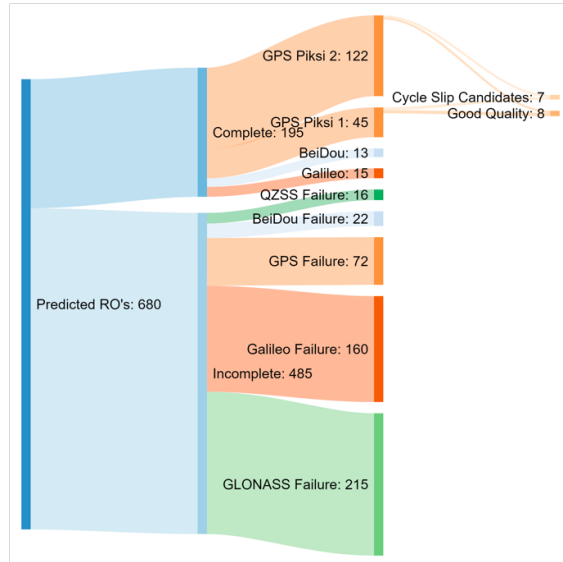
629
630   *Figure A1: Sankey filtering plot visualizing the balloon-borne RO case filtering from the World View field campaign.*

631   **8. References**

632   Adhikari, L., Xie, F., and Haase, J. S.: Application of the full spectrum inversion algorithm to
633   simulated airborne GPS radio occultation signals, Atmospheric Measurement Techniques, 9,
634   5077–5087, https://doi.org/10.5194/amt-9-5077-2016, 2016.

635   Anthes, R. A., Bernhardt, P. A., Chen, Y., Cucurull, L., Dymond, K. F., Ector, D., Healy, S. B.,
636   Ho, S. P., Hunt, D. C., Kuo, Y. H., Liu, H., Manning, K., McCormick, C., Meehan, T. K.,
637   Randel, W. J., Rocken, C., Schreiner, W. S., Sokolovskiy, S. V., Syndergaard, S., Thompson, D.
638   C., Trenberth, K. E., Wee, T. K., Yen, N. L., and Zeng, Z.: The COSMIC/FORMOSAT-3
639   Mission: Early Results, Bulletin of the American Meteorological Society, 89, 313–334,
640   https://doi.org/10.1175/bams-89-3-313, 2008.

641   Ao, C. O., Chan, T. K., Iijima, A., Li, J.-L., Mannucci, A. J., Teixeira, J., Tian, B., and Waliser,
642   D. E.: Planetary Boundary Layer Information from GPS Radio Occultation Measurements,
643   GRAS SAF Workshop on Applications of GPSRO Measurements, 123–131, 2008.

644   Ao, C. O., Hajj, G. A., Meehan, T. K., Dong, D., Iijima, B. A., Mannucci, A. J., and Kursinski,
645   E. R.: Rising and setting GPS occultations by use of open-loop tracking, Journal of Geophysical
646   Research, 114, https://doi.org/10.1029/2008jd010483, 2009.

648   Ao, C. O., Waliser, D. E., Chan, S. K., Li, J.-L., Tian, B., Xie, F., and Mannucci, A. J.: Planetary
649   boundary layer heights from GPS radio occultation refractivity and humidity profiles, Journal of
650   Geophysical Research: Atmospheres, 117, n/a-n/a, https://doi.org/10.1029/2012jd017598, 2012.

651   Boullot, N., Rabier, F., Langland, R., Gelaro, R., Cardinali, C., Guidard, V., Bauer, P., and
652   Doerenbecher, A.: Observation impact over the southern polar area during the Concordiasi field
653   campaign, Quarterly Journal of the Royal Meteorological Society, 142, 597–610,
654   https://doi.org/10.1002/qj.2470, 2014.

655   Bowler, N. E.: An assessment of GNSS radio occultation data produced by Spire, Quarterly
656   Journal of the Royal Meteorological Society, 146, 3772–3788, https://doi.org/10.1002/qj.3872,
657   2020.

658   Cao, B., Haase, J. S., Murphy, M. J., Alexander, M. J., Bramberger, M., and Hertzog, A.:
659   Equatorial waves resolved by balloon-borne Global Navigation Satellite System radio
660   occultation in the Strateole-2 campaign, Atmos. Chem. Phys., 22, 15379–15402,
661   https://doi.org/10.5194/acp-22-15379-2022, 2022.

662   Cardinali, C. and Healy, S.: Impact of GPS radio occultation measurements in the ECMWF
663   system using adjoint-based diagnostics: Impact of GPS radio occultation measurements, Q.J.R.
664   Meteorol. Soc., 140, 2315–2320, https://doi.org/10.1002/qj.2300, 2014.

665   Carreno-Luengo, H., Camps, A., Querol, J., and Forte, G.: First Results of a GNSS-R
666   Experiment From a Stratospheric Balloon Over Boreal Forests, IEEE Transactions on
667   Geoscience and Remote Sensing, 54, 2652–2663, https://doi.org/10.1109/tgrs.2015.2504242,
668   2016.

669   Chan, B. C., Goel, A., Kosh, J., Reid, T. G. R., Snyder, C. R., Tarantino, P. M., Soedarmadji, S.,
670   Soedarmadji, W., Nelson, K. J., Xie, F., and Vergalla, M.: GNSS Radio Occultation on Aerial
671   Platforms with Commercial Off-the-Shelf Receivers, ION GNSS Proceedings, 2021.

672   Chan, B. C., Goel, A., Kosh, J., Reid, T. G. R., Snyder, C. R., Tarantino, P. M., Soedarmadji, S.,
673   Soedarmadji, W., Nelson, K., Xie, F., and Vergalla, M.: Commercial GNSS Radio Occultation
674   on Aerial Platforms With Off-The-Shelf Receivers, navi, 69, navi.544,
675   https://doi.org/10.33012/navi.544, 2022a.

676   Fjeldbo, G. and Eshleman, V. R.: Atmosphere of Venus as Studied with the Mariner 5 Dual
677   Radio-Frequency Occultation Experiment, Radio Science, 4, 879–897,
678   https://doi.org/10.1029/RS004i010p00879, 1969.

679   Fjeldbo, G., Kliore, A. J., and Eshleman, V. R.: The neutral atmosphere of Venus as studied with
680   the Mariner V radio occultation experiments, The Astronomical Journal, 76, 123, 1971.

681   Garrison, J. L., Walker, M., Haase, J. S., Lulich, T., Xie, F., Ventre, B., Boehme, M. H.,
682   Wilmhoff, B., and Katzberg, S. J.: Development and Testing of the GISMOS Instrument, IEEE
683   International, 2007.

684   Gelaro, R.: GEOS-5 Data Assimilation and Forecast Impacts for Concordiasi, THORPEX DAOS
685   Working Group, 2011.

686   Haase, J. S., Maldonado-Vargas, J., Rabier, F., Cocquerez, P., Minois, M., Guidard, V., Wyss,
687   P., and Johnson, A. V.: A proof-of-concept balloon-borne Global Positioning System radio
688   occultation profiling instrument for polar studies, Geophysical Research Letters, 39, n/a-n/a,
689   https://doi.org/10.1029/2011gl049982, 2012.

690   Haase, J. S., Alexander, M. J., Hertzog, A., Kalnajs, L., Deshler, T., Davis, Sean M.,
691   Plougonven, R., Cocquerez, P., and Venel, S.: Around the World in 84 Days, EOS, 99, 2018.

692   Harnisch, F., Healy, S. B., Bauer, P., and English, S. J.: Scaling of GNSS Radio Occultation
693   Impact with Observation Number Using an Ensemble of Data Assimilations, Monthly Weather
694   Review, 141, 4395–4413, https://doi.org/10.1175/mwr-d-13-00098.1, 2013.

695   Healy, S. B., Haase, J. S., and Lesne, O.: Abel transform inversion of radio occultation
696   measurements made with a receiver inside the Earth's atmosphere, Annales Geophysicae, 20,
697   2002.

698   Hersbach, H., Bell, B., Berrisford, P., Hirahara, S., Horányi, A., Muñoz-Sabater, J., Nicolas, J.,
699   Peubey, C., Radu, R., Schepers, D., Simmons, A., Soci, C., Abdalla, S., Abellan, X., Balsamo,
700   G., Bechtold, P., Biavati, G., Bidlot, J., Bonavita, M., De Chiara, G., Dahlgren, P., Dee, D.,
701   Diamantakis, M., Dragani, R., Flemming, J., Forbes, R., Fuentes, M., Geer, A., Haimberger, L.,
702   Healy, S., Hogan, R. J., Hólm, E., Janisková, M., Keeley, S., Laloyaux, P., Lopez, P., Lupu, C.,
703   Radnoti, G., de Rosnay, P., Rozum, I., Vamborg, F., Villaume, S., and Thépaut, J.-N.: The ERA5
704   Global Reanalysis, Quarterly Journal of the Royal Meteorological Society, 146, 1999–2049,
705   https://doi.org/10.1002/qj.3803, 2020.

706   Ho, S., Anthes, R. A., Ao, C. O., Healy, S., Horanyi, A., Hunt, D., Mannucci, A. J., Pedatella,
707   N., Randel, W. J., Simmons, A., Steiner, A., Xie, F., Yue, X., and Zeng, Z.: The
708   COSMIC/FORMOSAT-3 Radio Occultation Mission after 12 Years: Accomplishments,
709   Remaining Challenges, and Potential Impacts of COSMIC-2, Bulletin of the American
710   Meteorological Society, 101, E1107–E1136, https://doi.org/10.1175/bams-d-18-0290.1, 2020.

711   Høeg, P., Hauchecorne, A., Kirchengast, G., Syndergaard, S., Belloul, B., Leitinger, R., and
712   Rothleitner, W.: Derivation of Atmospheric Properties using a Radio Occultation Technique,
713   Danish Meteorological Institute, Copenhagen, Denmark, 1996.

714   Imamura, T., Ando, H., Tellmann, S., Pätzold, M., Häusler, B., Yamazaki, A., Sato, T. M.,
715   Noguchi, K., Futaana, Y., Oschlisniok, J., Limaye, S., Choudhary, R. K., Murata, Y., Takeuchi,
716   H., Hirose, C., Ichikawa, T., Toda, T., Tomiki, A., Abe, T., Yamamoto, Z., Noda, H., Iwata, T.,
717   Murakami, S., Satoh, T., Fukuhara, T., Ogohara, K., Sugiyama, K., Kashimura, H., Ohtsuki, S.,
718   Takagi, S., Yamamoto, Y., Hirata, N., Hashimoto, G. L., Yamada, M., Suzuki, M., Ishii, N.,
719   Hayashiyama, T., Lee, Y. J., and Nakamura, M.: Initial performance of the radio occultation
720   experiment in the Venus orbiter mission Akatsuki, Earth, Planets and Space, 69,
721   https://doi.org/10.1186/s40623-017-0722-3, 2017.

722 Jensen, A. S., Lohmann, M. S., Benzon, H.-H., and Nielsen, A. S.: Full Spectrum Inversion of
723 radio occultation signals, Radio Science, 38, n/a-n/a, https://doi.org/10.1029/2002rs002763,
724 2003.

725 Kliore, A. J., Cain, D. L., Fjeldbo, G., Seidel, B. L., Sykes, M. J., and Rasool, S. I.: The
726 Atmosphere of Mars from Mariner 9 Radio Occultation Measurements, Icarus, 17, 484–516,
727 1972.

728 Kursinski, E. R., Hajj, G. A., Bertiger, W. I., Leroy, S. S., Meehan, T. K., Romans, L. J.,
729 Schofield, J. T., McCleese, D. J., Melbourne, W. G., Thornton, C. L., Yunck, T. P., Eyre, J. R.,
730 and Nagafini, R. N.: Initial Results of Radio Occultation Observations of Earth's Atmosphere
731 Using the Global Positioning System, Science, 271, 1107–1110, 1996.

732 Kursinski, E. R., Hajj, G. A., Schofield, J. T., Linfield, R. P., and Hardy, K. R.: Observing
733 Earth's atmosphere with radio occultation measurements using the Global Positioning System,
734 Journal of Geophysical Research: Atmospheres, 102, 23429–23465,
735 https://doi.org/10.1029/97jd01569, 1997.

736 Kursinski, E. R., Hajj, G. A., Leroy, S. S., and Herman, B.: The GPS Radio Occultation
737 Technique, Terrestrial, Atmospheric, and Oceanic Sciences, 11, 53–114, 2000.

738 Lesne, O., Haase, J. S., Kirchengast, G., Ramsauer, J., and Poetzi, W.: Sensitivity analysis for
739 airborne sounding of the troposphere by GNSS radio occultation, Physics and Chemistry of the
740 Earth, 27, 2002.

741 Lindal, G. F.: The atmosphere of Neptune-an analysis of radio occultation data acquired with
742 Voyager 2, The Astronomical Journal, 103, 967–982, 1992.

743 Lindal, G. F., Hotz, H. B., Sweetnam, D. N., Shippony, Z., Brenkle, J. P., Hartsell, G. V., Spear,
744 R. T., and Michael, W. H.: Viking radio occultation measurements of the atmosphere and
745 topography of Mars: Data acquired during 1 Martian year of tracking, Journal of Geophysical
746 Research, 84, https://doi.org/10.1029/JB084iB14p08443, 1979.

747 Luntama, J.-P., Kirchengast, G., Borsche, M., Foelsche, U., Steiner, A., Healy, S., von Engeln,
748 A., O'Clerigh, E., and Marquardt, C.: Prospects of the EPS GRAS Mission for Operational
749 Atmospheric Applications, Bulletin of the American Meteorological Society, 89, 1863–1875,
750 https://doi.org/10.1175/2008BAMS2399.1, 2008.

751 Murphy, B. J., Haase, J. S., Muradyan, P., Garrison, J. L., and Wang, K. N.: Airborne GPS radio
752 occultation refractivity profiles observed in tropical storm environments, Journal of Geophysical
753 Research: Atmospheres, 120, 1690–1709, https://doi.org/10.1002/2014jd022931, 2015.

754 National Academies of Sciences, E.: Thriving on Our Changing Planet: A Decadal Strategy for
755 Earth Observation from Space, The National Academies Press, Washington, DC, 2018.

756 NASA ESDS Commercial Smallsat Data Acquisition (CSDA) Program:
757 https://www.earthdata.nasa.gov/esds/csda, last access: 25 January 2023.

758 National Oceanic and Atmospheric Administration and National Environmental Satellite, Data,
759 and Information Service: Commercial Weather Data Pilot (CWDP) Round 2 Summary, 2020.

760 Nelson, K. J., Xie, F., Ao, C. O., and Oyola-Merced, M. I.: Diurnal Variation of the Planetary
761 Boundary Layer Height Observed from GNSS Radio Occultation and Radiosonde Soundings
762 over the Southern Great Plains, Journal of Atmospheric and Oceanic Technology, 38, 2081–
763 2093, https://doi.org/10.1175/jtech-d-20-0196.1, 2021.

764 Rabier, F., Bouchard, A., Brun, E., Doerenbecher, A., Guedj, S., Guidard, V., Karbou, F., Peuch,
765 V.-H., El Amraoui, L., Puech, D., Genthon, C., Picard, G., Town, M., Hertzog, A., Vial, F.,
766 Cocquerez, P., Cohn, S. A., Hock, T., Fox, J., Cole, H., Parsons, D., Powers, J., Romberg, K.,
767 VanAndel, J., Deshler, T., Mercer, J., Haase, J. S., Avallone, L., Kalnajs, L., Mechoso, C. R.,
768 Tangborn, A., Pellegrini, A., Frenot, Y., Thépaut, J.-N., McNally, A., Balsamo, G., and Steinle,
769 P.: The Concordiasi Project in Antarctica, Bulletin of the American Meteorological Society, 91,
770 69–86, https://doi.org/10.1175/2009bams2764.1, 2010.

771 Rabier, F., Cohn, S., Cocquerez, P., Hertzog, A., Avallone, L., Deshler, T., Haase, J., Hock, T.,
772 Doerenbecher, A., Wang, J., Guidard, V., Thépaut, J.-N., Langland, R., Tangborn, A., Balsamo,
773 G., Brun, E., Parsons, D., Bordereau, J., Cardinali, C., Danis, F., Escarnot, J.-P., Fourrié, N.,
774 Gelaro, R., Genthon, C., Ide, K., Kalnajs, L., Martin, C., Meunier, L.-F., Nicot, J.-M., Perttula,
775 T., Potts, N., Ragazzo, P., Richardson, D., Sosa-Sesma, S., and Vargas, A.: The Concordiasi
776 Field Experiment over Antarctica: First Results from Innovative Atmospheric Measurements,
777 Bulletin of the American Meteorological Society, 94, ES17–ES20, https://doi.org/10.1175/bams-
778 d-12-00005.1, 2013.

779 Ruston, B. and Healy, S.: Forecast Impact of FORMOSAT-7/COSMIC-2 GNSS Radio
780 Occultation Measurements, Atmospheric Science Letters, 22, https://doi.org/10.1002/asl.1019,
781 2020.

782 Schreiner, W. S., Weiss, J. P., Anthes, R. A., Braun, J., Chu, V., Fong, J., Hunt, D., Kuo, Y.-H.,
783 Meehan, T., Serafino, W., Sjoberg, J., Sokolovskiy, S., Talaat, E., Wee, T. K., and Zeng, Z.:
784 COSMIC-2 Radio Occultation Constellation: First Results, Geophysical Research Letters, 47,
785 https://doi.org/10.1029/2019gl086841, 2020.

786 Shi, J. Q. and Choi, T.: Gaussian Process Regression Analysis for Functional Data, CRC Press,
787 Boca Raton, FL, USA, 2011.

788 Vorob'ev, V. V. and Krasil'nikova, T. G.: Estimation of the Accuracy of the Atmospheric
789 Refractive Index Recovery from Doppler Shift Measurements at Frequencies Used in the
790 NAVSTAR System, Physics of the Atmosphere and Ocean, 29, 1994.

791 Wang, K.-N., Muradyan, P., Garrison, J. L., Haase, J. S., Murphy, B., Acikoz, U., and Lulich, T.:
792 Open-loop tracking of rising and setting GNSS radio-occultation signals from an Airborne
793 Platform: Signal model and statistical analysis, IGARSS Proceedings, 3367–3370,
794 https://doi.org/10.1109/IGARSS.2013.6723550, 2013.

795 Wang, K.-N., Garrison, J. L., Acikoz, U., Haase, J. S., Murphy, B. J., Muradyan, P., and Lulich,
796 T.: Open-Loop Tracking of Rising and Setting GPS Radio-Occultation Signals From an Airborne

797   Platform: Signal Model and Error Analysis, IEEE Transactions on Geoscience and Remote
798   Sensing, 54, 3967–3984, https://doi.org/10.1109/tgrs.2016.2532346, 2016.

799   Ware, R. H., Exner, M., Feng, D., Gorbunov, M., Hardy, K. R., Herman, B., Kuo, Y. H.,
800   Meehan, T. K., Melbourne, W., Rocken, C., Schreiner, W. S., Sokolovskiy, S., Solheim, F., Zou,
801   X., Anthes, R., Businger, S., and Trenberth, K. E.: GPS Sounding of the Atmosphere from Low
802   Earth Orbit: Preliminary Results, Bulletin of the American Meteorological Society, 77, 19–40,
803   1996.

804   Winning, T. E., Chen, Y.-L., and Xie, F.: Estimation of the marine boundary layer height over
805   the central North Pacific using GPS radio occultation, Atmospheric Research, 183, 362–370,
806   https://doi.org/10.1016/j.atmosres.2016.08.005, 2017.

807   Xie, F., Syndergaard, S., Kursinski, E. R., and Herman, B. M.: An approach for retrieving marine
808   boundary layer refractivity from GPS occultation data in the presence of superrefraction, Journal
809   of Atmospheric and Oceanic Technology, 23, 1629–1644, https://doi.org/10.1175/JTECH1996.1,
810   2006.

811   Xie, F., Haase, J. S., and Syndergaard, S.: Profiling the Atmosphere Using the Airborne GPS
812   Radio Occultation Technique: A Sensitivity Study, IEEE Transactions on Geoscience and
813   Remote Sensing, 46, 3424–3435, https://doi.org/10.1109/tgrs.2008.2004713, 2008.

814   Xie, F., Adhikari, L., Haase, J. S., Murphy, B., Wang, K.-N., and Garrison, J. L.: Sensitivity of
815   airborne radio occultation to tropospheric properties over ocean and land, Atmospheric
816   Measurement Techniques, 11, 763–780, https://doi.org/10.5194/amt-11-763-2018, 2018.

817   Zuffada, C., Hajj, G. A., and Kursinski, E. R.: A novel approach to atmospheric profiling with a
818   mountain-based or airborne GPS receiver, Journal of Geophysical Research: Atmospheres, 104,
819   24435–24447, https://doi.org/10.1029/1999jd900766, 1999.

820